Radiat Environ Biophys (2017) 56:453–462
DOI 10.1007/s00411-017-0705-6

ORIGINAL ARTICLE

Organ and effective dose rate coefficients for submersion exposure in occupational settings

K. G. Veinot[1,2] · S. A. Dewji[3] · M. M. Hiller[3] · K. F. Eckerman[1] · C. E. Easterly[1]

Received: 27 March 2017 / Accepted: 29 July 2017 / Published online: 24 August 2017

Abstract External dose coefficients for environmental exposure scenarios are often computed using assumption on infinite or semi-infinite radiation sources. For example, in the case of a person standing on contaminated ground, the source is assumed to be distributed at a given depth (or between various depths) and extending outwards to an essentially infinite distance. In the case of exposure to contaminated air, the person is modeled as standing within a cloud of infinite, or semi-infinite, source distribution. However, these scenarios do not mimic common workplace environments where scatter off walls and ceilings may significantly alter the energy spectrum and dose coefficients. In this paper, dose rate coefficients were calculated using the International Commission on Radiological Protection (ICRP) reference voxel phantoms positioned in rooms of three sizes representing an office, laboratory, and warehouse. For each room size calculations using the reference phantoms were performed for photons, electrons, and positrons as the source particles to derive mono-energetic dose rate coefficients. Since the voxel phantoms lack the resolution to perform dose calculations at the sensitive depth for the skin, a mathematical phantom was developed and calculations were performed in each room size with the three source particle types. Coefficients for the noble gas radionuclides of ICRP Publication 107 (e.g., Ne, Ar, Kr, Xe, and Rn) were generated by folding the corresponding photon, electron, and positron emissions over the mono-energetic dose rate coefficients. Results indicate that the smaller room sizes have a significant impact on the dose rate per unit air concentration compared to the semi-infinite cloud case. For example, for Kr-85 the warehouse dose rate coefficient is 7% higher than the office dose rate coefficient while it is 71% higher for Xe-133.

Keywords Organ dose · Effective dose · Room submersion · Air submersion

Introduction

International Commission on Radiological Protection (ICRP) Publication 116 (ICRP 2010) reports external dose coefficients for the reference voxel phantoms of ICRP Publication 110 (ICRP 2009) in so-called standard geometries (e.g., anterior–posterior, posterior–anterior, isotropic, etc.) computed according to the guidance of ICRP Publication 103 (ICRP 2007). External dose coefficients have also been reported for environmental scenarios such as submersion in radioactive clouds (Bellamy et al. 2016), immersion in contaminated water (Bellamy et al. 2016), and for persons standing on contaminated ground (Veinot et al. 2017). These cases, however, assume infinite or semi-infinite sources and do not include effects of scattering objects or boundaries such as walls or ceilings or ground surfaces other than soil. In the present work, dose rate coefficients calculated using reference voxel phantoms positioned in rooms of three sizes representing an office, laboratory, and warehouse are reported for photons, electrons, and positrons as the source particles. Since the voxel phantoms lack the resolution to perform dose calculations at the recommended depth for the

✉ K. G. Veinot
veinotkg@y12.doe.gov

[1] Easterly Scientific, 6412 Westminster Rd., Knoxville, TN 37919, USA

[2] Y-12 National Security Complex, P.O. Box 2009, Oak Ridge, TN 37831-8206, USA

[3] Oak Ridge National Laboratory, Center for Radiation Protection Knowledge, P.O. Box 2008, MS 6335, Oak Ridge, TN 37831-6335, USA

Table 1 ICRP Publication 110 (ICRP 2009) voxel phantom lattice characteristics

Property	Male	Female
Height (m)	1.76	1.63
Mass (kg)	73.0	60.0
Voxel dimension		
Z direction (mm)[a]	8.0	4.84
X- and *Y*-direction (mm)	2.137	1.775
Voxel volume (mm^3)	36.54	15.25
Number of voxels along *X*-axis	254	299
Number of voxels along *Y*-axis	127	137
Number of voxels along *Z*-axis	222	348
Number of tissue voxels	1,950,255	3,887,730
Number of void voxels	5,211,021	10,367,394
Total number of voxels	7,161,276	14,255,124

[a] Axis orientation: *X*-axis right to left; *Y*-axis front to back; *Z*-axis feet to head

skin, a simple mathematical phantom was substituted and calculations were repeated in each room size with the three source particle types. Occupational radiation protection guidance limiting airborne concentrations of noble gases at the work place were developed as detailed in ICRP Publication 30, Part 1 (ICRP 1979). That approach increased the semi-infinite cloud dose coefficient by a factor of two, as the exposure geometry in the room is infinite, and applied an energy-dependent factor involving the product of the radius of a sphere equal to the volume of the room and the photon mass energy absorption coefficient in air. Those calculations were intended to simulate rooms of various sizes; however, the simulations lacked physical features such as walls, floors, and ceilings.

Materials and methods

Protection quantity calculations in ICRP Publication 103

As in previous ICRP recommendations such as ICRP Publication 26 (ICRP 1977) and ICRP Publication 60 (ICRP 1991), the method for determining protection quantities begins with calculating doses to organs and tissues using appropriate reference phantoms. The ICRP Publication 103 (ICRP 2007) guidance requires that organ and tissue equivalent dose be determined for the organs and tissues of the adult reference male and female voxel phantom separately and then the sex-averaged equivalent doses be derived. The radiation weighting factors, w_R, given in ICRP Publication 103 for photons, electrons, and positrons are assigned a value of unity. Once the sex-averaged equivalent doses are determined, they are weighted using the tissue weighting factors and the tissue-weighted equivalent doses summed to determine the effective dose (Eqs. 1, 2).

$$H_T = \sum_R w_R D_{T,R}, \tag{1}$$

where H_T is the tissue or organ equivalent dose, w_R is the radiation weighting factor and $D_{T,R}$ is the absorbed dose to tissue or organ T from radiation R.

$$E = \sum_T w_T \left[\frac{H_T^M + H_T^F}{2} \right], \tag{2}$$

where E is the effective dose, H_T^M is the equivalent dose to organ T of the male phantom, H_T^F is the equivalent dose to organ T of the female phantom, and w_T is the organ or tissue weighting factor.

Reference phantoms

The reference phantoms of ICRP Publication 110 (ICRP 2009) were used for all organ and tissue calculations with the exception of the skin as will be discussed later. These three-dimensional phantoms are voxel-based representations of male and female subjects produced via high-resolution computed tomography (CT) scans. The male phantom consists of about 7.2 million voxels of which about 2.0 million represent tissues. Each voxel is a rectangular prism being 8 mm × 2.137 mm × 2.137 mm. The female phantom consists of about 14 million voxels of which about 3.9 million represent tissues. The dimension of the female voxel is 4.84 mm × 1.775 mm × 1.775 mm. The tissue compositions and densities are based on ICRP Publication 89 (ICRP 2002) information and the non-tissue voxels are voids. The male phantom is 1.76 m in height and has a mass of 73 kg while the female is 1.63 m tall and has a mass of 60 kg. Because of the voxel resolution, exact calculations to basal cell regions of the skin are not possible. Some characteristics of the ICRP Publication 110 phantoms are listed in Table 1.

Mathematical phantom for skin calculations

The voxel size of the reference phantoms does not allow for dose calculations at the sensitive cells of the skin (assumed to be at an average depth of 70 μm). To perform absorbed dose calculations at the sensitive depth, a mathematical representation was developed for this work consisting of a cylinder 20 cm in radius and 153 cm in height. Additionally, a hemisphere having radius of 20 cm was placed at the top of the cylinder. A thin volume (40 μm thick) was centered at a depth of 70 μm beneath the phantom outer edge along the cylinder and hemisphere. Thus, the calculated dose in the

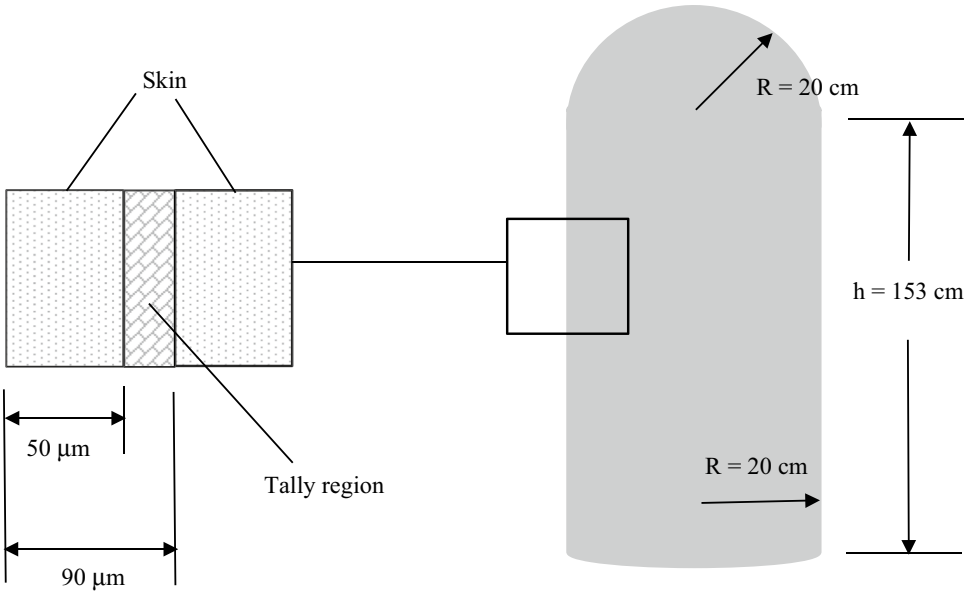

Fig. 1 Depiction of skin phantom. This phantom was used for skin dose calculations and tallied the deposition between 50 and 90 µm

Table 2 Room dimensions and geometry

Room description	Dimensions (m)	Volume (m^3)	Composition
Small (office)	5.8 × 5.8 × 3.0	100.92	Walls and ceiling 2.54 cm (1-inch) concrete 1.27 cm (½-inch) sheet rock Floor 30 cm concrete
Medium (laboratory)	10 × 20 × 30	600	Walls and ceiling 2.54 cm (1-inch) concrete 1.27 cm (½-inch) sheet rock Floor 30 cm concrete
Large (warehouse)	15 × 15 × 5.3	~1192	Walls and ceiling 20.32 cm (8-inches) concrete No sheetrock Floor 30 cm concrete

region between 50 and 90 µm depth was used as a surrogate for the skin dose for effective dose calculations. This region differs slightly from that used in ICRP 116 (50–100 µm depth), but was chosen since it provides equal thickness above and below the 70 µm reference. The skin phantom is depicted in Fig. 1.

Room descriptions

Three room sizes were investigated. The first, representing an office, was 5.8 m in length and width, and had a ceiling height of 3 m; resulting in a volume of 100 m^3. The walls and ceiling were modeled as one half inch thick sheetrock (gypsum), with one inch thick ordinary concrete (ρ = 2.35 g cm^{-3}) behind the sheetrock. The floor was a 30 cm thick concrete slab. All material compositions and densities were taken from (McConn et al. 2011). The laboratory dimensions were 10 m wide, 20 m in depth, with a ceiling height of 3 m and a corresponding volume of 600 m^3. Wall, floor, and ceiling compositions were identical to those modeled for the office scenario. The warehouse dimensions were 15 m wide, 15 m in depth, with a ceiling height of 5.3 m with walls similar to those for the office and laboratory, the volume of the warehouse being 1192 m^3. The room geometry specifications and composition are summarized in Table 2. For each room size, the interior volume was assumed to be air having a density of 1.2 kg m^{-3}. The phantom was centered in the rooms standing upright on the floor (Fig. 2). Source particles were sampled uniformly within the air volume. The dimensions chosen to be representative of an office, laboratory, and warehouse, are similar to those considered in ICRP Publication 30 (ICRP 79).

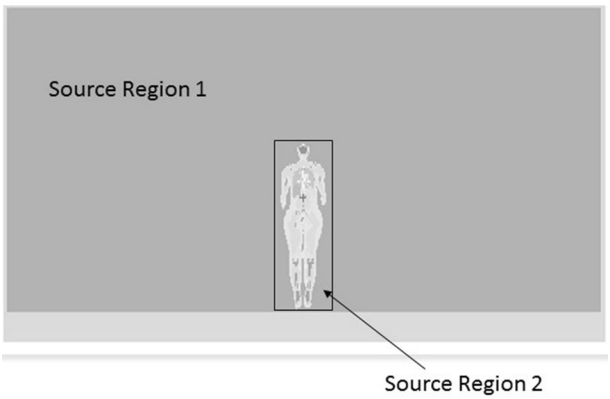

Fig. 2 Depiction of adult female voxel phantom in office setting. Calculations were performed in two steps. The first step generated source particles inside the room and outside the *box* surrounding the phantom (region 1 in the figure). The second generated source particles only inside the *box* (region 2 in the figure)

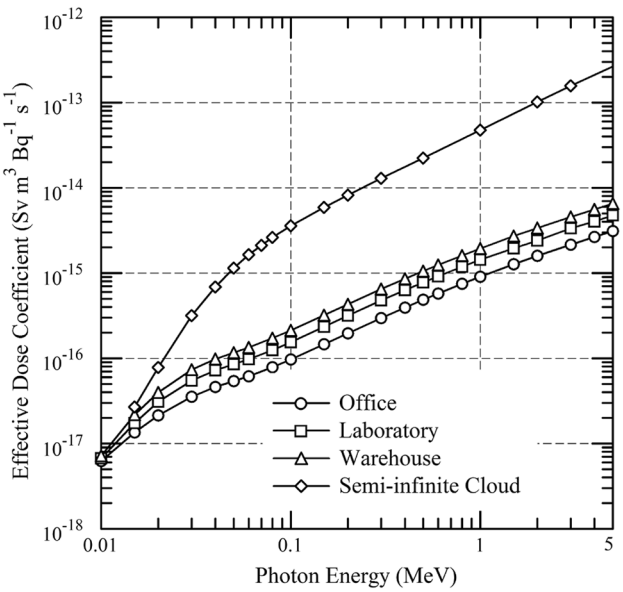

Fig. 3 Photon effective dose rate coefficients for the office, laboratory, and warehouse. Also shown are coefficients for the male and female voxel phantoms immersed in a semi-infinite cloud as reported in (Petoussi-Henss et al. 2012)

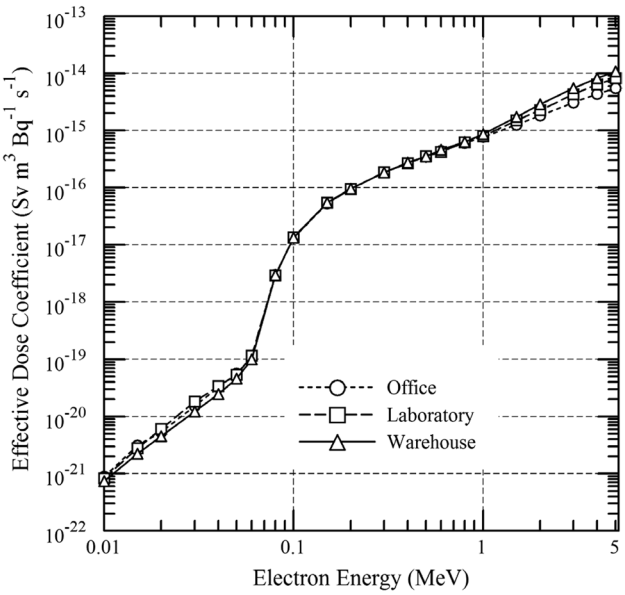

Fig. 4 Electron effective dose rate coefficients for the office, laboratory, and warehouse

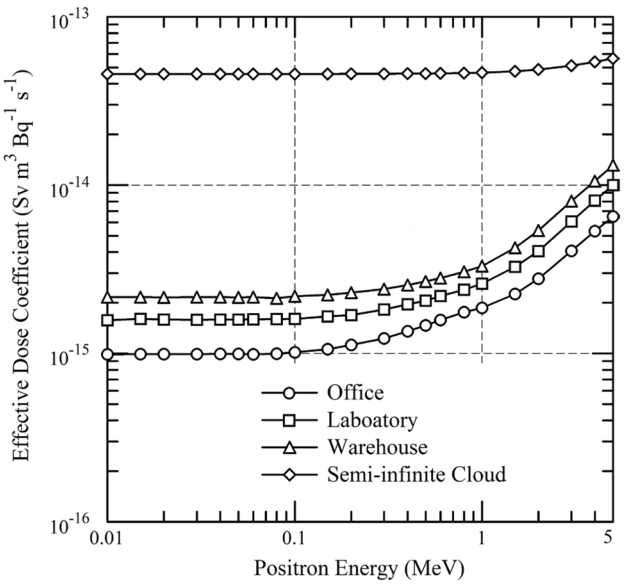

Fig. 5 Positron effective dose rate coefficients for the office, laboratory, and warehouse. Also shown are the coefficients for the male and female voxel phantoms immersed in a semi-infinite cloud

Calculation method

Calculations were performed using the MCNP6.1 (MCNP 2013) radiation transport code along with the ENDF/B-VI (ENDF 2005) cross sections. Absorbed doses to the organs were computed by tracking the charged particle deposition within the respective tally volumes. Bremsstrahlung and annihilation photon production was included and tracked. The derived organ and tissue doses were normalized to the total source volume (room air volume less the volume of the phantom).

The phantoms, as defined in (ICRP 2009), are within a rectangular prism consisting of voxels representing tissue and voxels outside the body defined as voids. In the present application, these voids were redefined as air (about 73% of the voxels of either phantom). Two sets of calculations were

Table 3 Photon effective dose rate coefficients for the office, laboratory, and warehouse

Energy (MeV)	Effective dose rate coefficient (Sv m^3 Bq^{-1} s^{-1}). Error is the propagated uncertainty of effective dose based on the Monte-Carlo tally error in the organ and tissue doses (as reported by MCNP)					
	Office		Laboratory		Warehouse	
	Value	Error	Value	Error	Value	Error
0.01	6.235×10^{-18}	5.146×10^{-20}	6.701×10^{-18}	5.939×10^{-20}	7.186×10^{-18}	5.210×10^{-20}
0.015	1.351×10^{-17}	8.605×10^{-20}	1.742×10^{-17}	1.555×10^{-19}	2.176×10^{-17}	1.013×10^{-19}
0.02	2.141×10^{-17}	8.876×10^{-20}	3.086×10^{-17}	2.278×10^{-19}	3.992×10^{-17}	1.323×10^{-19}
0.03	3.553×10^{-17}	1.028×10^{-19}	5.495×10^{-17}	3.051×10^{-19}	7.341×10^{-17}	1.721×10^{-19}
0.04	4.600×10^{-17}	1.445×10^{-19}	7.220×10^{-17}	3.489×10^{-19}	9.800×10^{-17}	1.963×10^{-19}
0.05	5.416×10^{-17}	1.797×10^{-19}	8.537×10^{-17}	3.886×10^{-19}	1.167×10^{-16}	2.381×10^{-19}
0.06	6.169×10^{-17}	2.149×10^{-19}	9.760×10^{-17}	4.125×10^{-19}	1.344×10^{-16}	2.898×10^{-19}
0.08	7.868×10^{-17}	2.978×10^{-19}	1.244×10^{-16}	4.588×10^{-19}	1.722×10^{-16}	3.957×10^{-19}
0.1	9.704×10^{-17}	3.776×10^{-19}	1.542×10^{-16}	5.155×10^{-19}	2.122×10^{-16}	4.930×10^{-19}
0.15	1.465×10^{-16}	2.260×10^{-19}	2.353×10^{-16}	6.942×10^{-19}	3.219×10^{-16}	7.920×10^{-19}
0.2	1.966×10^{-16}	3.016×10^{-19}	3.171×10^{-16}	9.112×10^{-19}	4.313×10^{-16}	1.088×10^{-18}
0.3	2.965×10^{-16}	4.871×10^{-19}	4.772×10^{-16}	1.706×10^{-18}	6.488×10^{-16}	1.660×10^{-18}
0.4	3.935×10^{-16}	6.771×10^{-19}	6.316×10^{-16}	2.431×10^{-18}	8.555×10^{-16}	2.255×10^{-18}
0.5	4.870×10^{-16}	8.831×10^{-19}	7.776×10^{-16}	3.148×10^{-18}	1.054×10^{-15}	3.142×10^{-18}
0.6	5.772×10^{-16}	1.091×10^{-18}	9.185×10^{-16}	5.033×10^{-18}	1.245×10^{-15}	4.097×10^{-18}
0.8	7.471×10^{-16}	1.480×10^{-18}	1.188×10^{-15}	1.001×10^{-17}	1.607×10^{-15}	6.215×10^{-18}
1	9.068×10^{-16}	1.859×10^{-18}	1.434×10^{-15}	1.232×10^{-17}	1.944×10^{-15}	8.539×10^{-18}
1.5	1.270×10^{-15}	2.789×10^{-18}	1.957×10^{-15}	1.311×10^{-17}	2.727×10^{-15}	1.502×10^{-17}
2	1.594×10^{-15}	3.648×10^{-18}	2.409×10^{-15}	3.600×10^{-17}	3.377×10^{-15}	2.120×10^{-17}
3	2.154×10^{-15}	5.296×10^{-18}	3.354×10^{-15}	4.591×10^{-17}	4.569×10^{-15}	3.494×10^{-17}
4	2.648×10^{-15}	7.564×10^{-18}	4.031×10^{-15}	4.345×10^{-17}	5.581×10^{-15}	4.693×10^{-17}
5	3.108×10^{-15}	9.464×10^{-18}	4.765×10^{-15}	7.001×10^{-17}	6.530×10^{-15}	5.990×10^{-17}

performed for each particle type. The first included the modeling of the source uniformly distributed inside the room, but outside the rectangular prism and labeled as source region 1 in Fig. 2. The second involved modeling of the source inside the rectangular prism enclosing the phantom and external to the phantom (volume 0.190 and 0.158 m^3 in the male and female, respectively). This is labeled as source region 2 in Fig. 2. The results of the two calculations were combined to produce the final set of dose rate coefficients.

Because of the segmentation of the cortical (bone surface) and spongiosa (red bone marrow) regions, these doses were tallied individually and mass weighted to determine the total bone surface and red bone marrow doses. This method is in accordance with that used for ICRP Publication 116 (ICRPs 2010).

Tally uncertainties were minimized (>2%), although some organs that received small doses had large tally uncertainties (<10%). In cases where these organs and tissues did not significantly contribute to the effective dose, this uncertainty was accepted without performing additional particle histories. In the cases of the bone surface and the red bone marrow, the contributor tally uncertainties were combined using mass weighting for each.

Generation of radionuclide dose rate coefficients

Radionuclide specific dose rate coefficients, $\dot{h}_T^S$, for tissue T and exposure mode, S, were computed as:

$$\dot{h}_T^S = \sum_{j=e^-,e^+,\gamma} \left[\sum_i Y_j(E_i)\hat{h}_{T,j}^S(E_i) + \int_0^\infty Y_j(E)\hat{h}_{T,j}^S(E)\mathrm{d}E \right], \quad (3)$$

where the outer summation extends over electron, positron, and photon radiations emitted by the investigated radionuclide. The first term within the major bracket sums over all radiation i of type j emitted with yield $Y_j(E_i)$ and energy E_i. The integral is over the continuous beta spectra. The quantity $\hat{h}_{T,j}^S(E_i)$ is the mono-energetic dose rate coefficient for radiation type j and tissue T. The energies of the simulated particles ranged from 10 keV to 5 MeV, with the lower energies corresponding to those used in (ICRP 2010). The yields of the various radiation types in the decay of the radionuclide were those tabulated in (ICRP 2008). Nuclide-specific dose rate coefficients were based on the mono-energetic dose rate coefficients for each of the room size, phantoms, and particle

Table 4 Electron effective dose rate coefficients for the office, laboratory, and warehouse

Energy (MeV)	Effective dose rate coefficient (Sv m^3 Bq^{-1} s^{-1}). Error is the propagated uncertainty of effective dose based on the Monte-Carlo tally error in the organ and tissue doses (as reported by MCNP)					
	Office		Laboratory		Warehouse	
	Value	Error	Value	Error	Value	Error
0.01	8.916×10^{-22}	1.496×10^{-22}	8.299×10^{-22}	1.556×10^{-22}	7.364×10^{-22}	1.490×10^{-22}
0.015	3.100×10^{-21}	4.317×10^{-22}	2.795×10^{-21}	2.198×10^{-22}	2.236×10^{-21}	2.012×10^{-23}
0.02	5.336×10^{-21}	9.943×10^{-23}	6.062×10^{-21}	6.693×10^{-22}	4.519×10^{-21}	3.286×10^{-23}
0.03	1.521×10^{-20}	4.072×10^{-22}	1.833×10^{-20}	2.117×10^{-21}	1.225×10^{-20}	6.564×10^{-23}
0.04	3.252×10^{-20}	1.301×10^{-21}	3.409×10^{-20}	1.785×10^{-21}	2.477×10^{-20}	1.078×10^{-22}
0.05	5.713×10^{-20}	2.229×10^{-21}	5.353×10^{-20}	1.001×10^{-21}	4.610×10^{-20}	4.676×10^{-22}
0.06	1.098×10^{-19}	1.726×10^{-21}	1.172×10^{-19}	2.754×10^{-21}	1.004×10^{-19}	1.344×10^{-21}
0.08	2.988×10^{-18}	6.979×10^{-20}	2.907×10^{-18}	3.726×10^{-20}	2.936×10^{-18}	6.734×10^{-20}
0.1	1.304×10^{-17}	3.386×10^{-19}	1.346×10^{-17}	3.846×10^{-19}	1.322×10^{-17}	1.661×10^{-19}
0.15	5.323×10^{-17}	7.434×10^{-19}	5.435×10^{-17}	1.160×10^{-18}	5.408×10^{-17}	1.205×10^{-18}
0.2	9.516×10^{-17}	9.989×10^{-19}	9.500×10^{-17}	2.003×10^{-18}	9.636×10^{-17}	1.744×10^{-18}
0.3	1.825×10^{-16}	1.419×10^{-18}	1.873×10^{-16}	3.368×10^{-18}	1.838×10^{-16}	2.334×10^{-18}
0.4	2.664×10^{-16}	1.786×10^{-18}	2.674×10^{-16}	5.900×10^{-18}	2.750×10^{-16}	4.222×10^{-18}
0.5	3.485×10^{-16}	5.004×10^{-18}	3.560×10^{-16}	6.863×10^{-18}	3.507×10^{-16}	2.758×10^{-18}
0.6	4.375×10^{-16}	5.206×10^{-18}	4.225×10^{-16}	1.075×10^{-17}	4.548×10^{-16}	7.978×10^{-18}
0.8	6.060×10^{-16}	3.202×10^{-18}	6.182×10^{-16}	1.459×10^{-17}	6.297×10^{-16}	1.076×10^{-17}
1	7.766×10^{-16}	7.779×10^{-18}	7.920×10^{-16}	1.718×10^{-17}	8.634×10^{-16}	7.997×10^{-18}
1.5	1.258×10^{-15}	1.092×10^{-17}	1.492×10^{-15}	2.235×10^{-17}	1.712×10^{-15}	1.548×10^{-17}
2	1.819×10^{-15}	1.104×10^{-17}	2.279×10^{-15}	3.918×10^{-17}	2.857×10^{-15}	2.416×10^{-17}
3	3.071×10^{-15}	1.670×10^{-17}	4.297×10^{-15}	9.027×10^{-17}	5.477×10^{-15}	4.297×10^{-17}
4	4.373×10^{-15}	3.555×10^{-17}	6.440×10^{-15}	1.412×10^{-16}	8.203×10^{-15}	6.565×10^{-17}
5	5.513×10^{-15}	4.298×10^{-17}	8.153×10^{-15}	1.279×10^{-16}	1.082×10^{-14}	8.678×10^{-17}

types using the ICRP Publication 107 nuclear decay data. The coefficients are based on the radiations emitted by the radionuclide with no consideration of possible radioactive progeny; see ICRP Publication 107 for details.

Results and discussion

Photon effective dose rate coefficients for the office, laboratory, and warehouse are shown in Fig. 3 along with coefficients for the male and female phantom immersed in a semi-infinite cloud reported in (Petoussi-Henss et al. 2012). At energies greater than 15 keV, the dose rate coefficient of the semi-infinite cloud is significantly higher than that of the warehouse. The mean free paths in air of photons with energies greater than about 15 keV are longer than the phantom-to-wall distance of the warehouse. Therefore, these photons contribute to the effective dose rate in the semi-infinite cloud scenario at distances greater than the largest room dimension studied here, resulting in a larger dose rate coefficient. At energies below 15 keV, the skin is the primary contributor to effective dose, where the semi-infinite coefficients are slightly smaller than those of the office, laboratory, or warehouse. This is a result of the skin models within the phantoms. For the stylized phantom used in (Bellamy et al. 2016), the skin is about 2 mm thick. Thus, the energy deposited by these low energy photons is averaged over a much larger volume (and corresponding mass) than in the mathematical phantom used in the present work. In addition, at energies below 60 keV, the semi-infinite cloud becomes infinite and thus the assumed one-half factor used in (Bellamy et al. 2016) results in an underestimate (see for example Ryman et al. 1981). The use of the kerma approximation in (Bellamy et al. 2016) differs with the approach used in the present work (where secondary charged particles were tracked). For higher photon energies, the lack of charged particle equilibrium will result in differences in some organ doses. These effects, however, are minimized by the source geometry and distribution of the organs, especially the skin which surrounds the phantom.

Effective dose rate coefficients for the three room sizes are shown in Fig. 4 for electrons and in Fig. 5 for positrons. Also shown in Fig. 5 are effective dose rate coefficients for the male and female phantoms immersed in a semi-infinite

Table 5 Positron effective dose rate coefficients for the office, laboratory, and warehouse

Energy (MeV)	Effective dose rate coefficient (Sv m^3 Bq^{-1} s^{-1}). Error is the propagated uncertainty of effective dose based on the Monte-Carlo tally error in the organ and tissue doses (as reported by MCNP)					
	Office		Laboratory		Warehouse	
	Value	Error	Value	Error	Value	Error
0.01	9.874×10^{-16}	3.385×10^{-18}	1.575×10^{-15}	8.799×10^{-18}	2.160×10^{-15}	6.304×10^{-18}
0.015	9.911×10^{-16}	3.692×10^{-18}	1.604×10^{-15}	9.744×10^{-18}	2.158×10^{-15}	6.294×10^{-18}
0.02	9.920×10^{-16}	3.349×10^{-18}	1.591×10^{-15}	8.431×10^{-18}	2.154×10^{-15}	6.227×10^{-18}
0.03	9.915×10^{-16}	4.192×10^{-18}	1.586×10^{-15}	8.440×10^{-18}	2.159×10^{-15}	6.356×10^{-18}
0.04	9.941×10^{-16}	3.696×10^{-18}	1.592×10^{-15}	1.050×10^{-17}	2.158×10^{-15}	6.205×10^{-18}
0.05	9.934×10^{-16}	3.416×10^{-18}	1.591×10^{-15}	7.692×10^{-18}	2.153×10^{-15}	1.406×10^{-17}
0.06	9.886×10^{-16}	4.499×10^{-18}	1.595×10^{-15}	9.326×10^{-18}	2.158×10^{-15}	1.410×10^{-17}
0.08	9.956×10^{-16}	4.113×10^{-18}	1.600×10^{-15}	1.205×10^{-17}	2.129×10^{-15}	1.350×10^{-17}
0.1	1.015×10^{-15}	3.823×10^{-18}	1.604×10^{-15}	1.121×10^{-17}	2.189×10^{-15}	1.312×10^{-17}
0.15	1.061×10^{-15}	2.671×10^{-18}	1.658×10^{-15}	1.297×10^{-17}	2.230×10^{-15}	1.454×10^{-17}
0.2	1.123×10^{-15}	3.816×10^{-18}	1.692×10^{-15}	1.034×10^{-17}	2.295×10^{-15}	6.900×10^{-18}
0.3	1.229×10^{-15}	3.630×10^{-18}	1.828×10^{-15}	1.167×10^{-17}	2.413×10^{-15}	1.547×10^{-17}
0.4	1.355×10^{-15}	6.440×10^{-18}	1.960×10^{-15}	1.708×10^{-17}	2.549×10^{-15}	1.554×10^{-17}
0.5	1.470×10^{-15}	3.164×10^{-18}	2.060×10^{-15}	1.521×10^{-17}	2.683×10^{-15}	1.430×10^{-17}
0.6	1.578×10^{-15}	1.001×10^{-17}	2.193×10^{-15}	1.804×10^{-17}	2.807×10^{-15}	1.832×10^{-17}
0.8	1.760×10^{-15}	9.163×10^{-18}	2.392×10^{-15}	2.176×10^{-17}	3.057×10^{-15}	2.058×10^{-17}
1	1.867×10^{-15}	1.245×10^{-17}	2.600×10^{-15}	2.364×10^{-17}	3.300×10^{-15}	2.542×10^{-17}
1.5	2.253×10^{-15}	1.371×10^{-17}	3.266×10^{-15}	2.357×10^{-17}	4.248×10^{-15}	3.629×10^{-17}
2	2.781×10^{-15}	3.276×10^{-17}	4.051×10^{-15}	3.778×10^{-17}	5.381×10^{-15}	7.671×10^{-17}
3	4.073×10^{-15}	2.442×10^{-17}	6.073×10^{-15}	7.845×10^{-17}	8.032×10^{-15}	1.418×10^{-16}
4	5.325×10^{-15}	2.888×10^{-17}	8.079×10^{-15}	1.591×10^{-16}	1.058×10^{-14}	1.471×10^{-16}
5	6.508×10^{-15}	3.434×10^{-17}	9.991×10^{-15}	1.507×10^{-16}	1.313×10^{-14}	1.707×10^{-16}

cloud. Tables 3, 4 and 5 list the energy-dependent effective dose rate coefficients for photons, electrons, and positrons, respectively. The impact of the smaller room size is evident in Fig. 3. For electrons and positrons this effect is seen as well. At energies between about 150 keV and 1 MeV, the positron and electron skin dose rate coefficients are similar for each of the three room sizes since the charged particles have adequate range to deposit energy at the 0.007 cm depth. At energies above about 1 MeV, the charged particles have energies allowing them to penetrate sufficiently deep so that all of their energy is not completely deposited at the sensitive depth and some room size effects are observed since the higher energy electrons have adequate range to reach the phantom as the room size increases. At energies less than about 150 keV, the majority of the dose is no longer a result of direct deposition by the charged particle, but instead by the positron annihilation. The produced annihilation photons can reach the phantom regardless of the room size so the resulting dose rate coefficients tend to remain constant to the lowest energy considered here. The positron skin dose rate coefficients at these low energies are approximately twice that of 500 keV photons since the probability of interaction is twice that of the photons as a result of the dual photon creation in the positron–electron annihilation process. Effective dose rate coefficients for positrons can be reasonably approximated by summing the electron dose rate coefficient and twice the 500 keV photon coefficient. Table 6 lists values for selected radionuclides distributed in the office, laboratory, and warehouse.[1]

In the case of photons, the ratio of dose rate coefficients for the warehouse to those for the office is about 2.2 for most energies. For electrons, the ratio increases significantly above 1 MeV and positrons are approximated by the combination of the electron coefficients and twice that of 500 keV photons. Kr-76 showed the largest dependence on room size with the coefficient of the warehouse being 2.17 times that of the office and the lab coefficient 1.6 times the office coefficient. In all cases, the ratios between warehouse and office were greater than those between lab and office and between the warehouse and lab except for Ar-42 and Kr-85. For these two nuclides, the ratio of coefficients was very close to one as the dose rate to skin dominates their effective dose rate coefficients.

[1] Tables for other organ and tissue coefficients are available for download at the Center for Radiation Protection Knowledge at http://crpk.ornl.gov/resources/ or by contacting the authors.

Table 6 Radionuclide effective dose rate coefficients for the office, laboratory, and warehouse

Nuclide	Effective dose rate coefficient (Sv m^3 Bq^{-1} s^{-1})		
	Office	Laboratory	Warehouse
Ne-19	1.83×10^{-15}	2.60×10^{-15}	3.36×10^{-15}
Ne-24	1.15×10^{-15}	1.51×10^{-15}	1.78×10^{-15}
Ar-39	1.19×10^{-16}	1.21×10^{-16}	1.22×10^{-16}
Ar-41	1.44×10^{-15}	2.06×10^{-15}	2.73×10^{-15}
Ar-42	1.30×10^{-16}	1.32×10^{-16}	1.35×10^{-16}
Ar-43	2.51×10^{-15}	3.53×10^{-15}	4.47×10^{-15}
Ar-44	2.00×10^{-15}	2.88×10^{-15}	3.87×10^{-15}
Kr-74	1.55×10^{-15}	2.23×10^{-15}	2.90×10^{-15}
Kr-75	2.63×10^{-15}	3.85×10^{-15}	5.07×10^{-15}
Kr-76	4.19×10^{-16}	6.70×10^{-16}	9.08×10^{-16}
Kr-77	1.60×10^{-15}	2.29×10^{-15}	2.98×10^{-15}
Kr-79	2.59×10^{-16}	4.04×10^{-16}	5.44×10^{-16}
Kr-81	5.53×10^{-18}	6.88×10^{-18}	8.36×10^{-18}
Kr-81 m	1.53×10^{-16}	2.31×10^{-16}	3.05×10^{-16}
Kr-83 m	1.58×10^{-18}	1.92×10^{-18}	2.31×10^{-18}
Kr-85	1.48×10^{-16}	1.51×10^{-16}	1.58×10^{-16}
Kr-85 m	3.09×10^{-16}	4.03×10^{-16}	5.00×10^{-16}
Kr-87	1.83×10^{-15}	2.48×10^{-15}	2.93×10^{-15}
Kr-88	1.83×10^{-15}	2.70×10^{-15}	3.64×10^{-15}
Kr-89	2.83×10^{-15}	4.05×10^{-15}	5.23×10^{-15}
Xe-120	3.95×10^{-16}	6.25×10^{-16}	8.44×10^{-16}
Xe-121	1.79×10^{-15}	2.66×10^{-15}	3.55×10^{-15}
Xe-122	7.22×10^{-17}	1.14×10^{-16}	1.53×10^{-16}
Xe-123	7.44×10^{-16}	1.10×10^{-15}	1.47×10^{-15}
Xe-125	2.79×10^{-16}	4.40×10^{-16}	5.95×10^{-16}
Xe-127	2.90×10^{-16}	4.59×10^{-16}	6.19×10^{-16}
Xe-127 m	2.04×10^{-16}	3.05×10^{-16}	4.02×10^{-16}
Xe-129 m	1.26×10^{-16}	1.59×10^{-16}	1.91×10^{-16}
Xe-131 m	6.85×10^{-17}	8.23×10^{-17}	9.40×10^{-17}
Xe-133	8.07×10^{-17}	1.09×10^{-16}	1.38×10^{-16}
Xe-133 m	1.35×10^{-16}	1.60×10^{-16}	1.85×10^{-16}
Xe-135	4.44×10^{-16}	5.94×10^{-16}	7.44×10^{-16}
Xe-135 m	4.83×10^{-16}	7.30×10^{-16}	9.70×10^{-16}
Xe-137	1.73×10^{-15}	2.27×10^{-15}	2.54×10^{-15}
Xe-138	1.45×10^{-15}	2.02×10^{-15}	2.59×10^{-15}
Rn-207	1.12×10^{-15}	1.71×10^{-15}	2.30×10^{-15}
Rn-209	1.18×10^{-15}	1.83×10^{-15}	2.47×10^{-15}
Rn-210	6.06×10^{-17}	9.46×10^{-17}	1.27×10^{-16}
Rn-211	1.73×10^{-15}	2.72×10^{-15}	3.70×10^{-15}
Rn-212	3.25×10^{-19}	5.15×10^{-19}	6.96×10^{-19}
Rn-218	7.37×10^{-19}	1.17×10^{-18}	1.58×10^{-18}
Rn-219	6.10×10^{-17}	9.61×10^{-17}	1.29×10^{-16}
Rn-220	6.18×10^{-19}	9.80×10^{-19}	1.33×10^{-18}
Rn-222	3.86×10^{-19}	6.11×10^{-19}	8.26×10^{-19}
Rn-223	7.29×10^{-16}	9.32×10^{-16}	1.11×10^{-15}

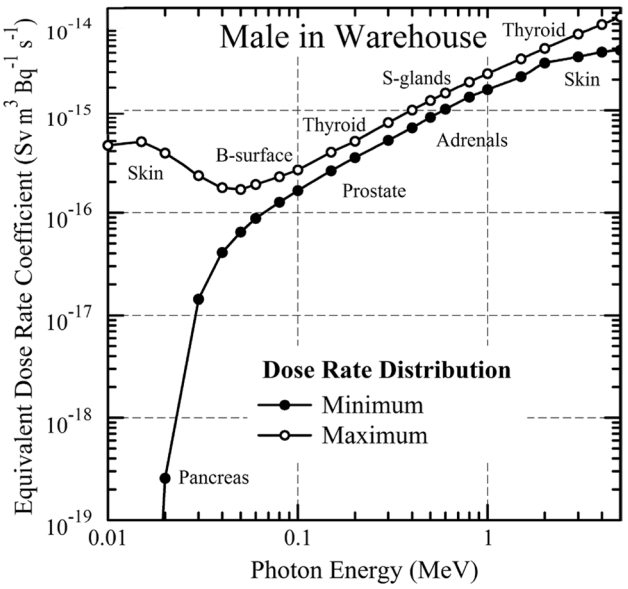

Fig. 6 Maximum and minimum dose rate coefficients for specific organs and tissues as a function of photon energy for the male phantom in the warehouse

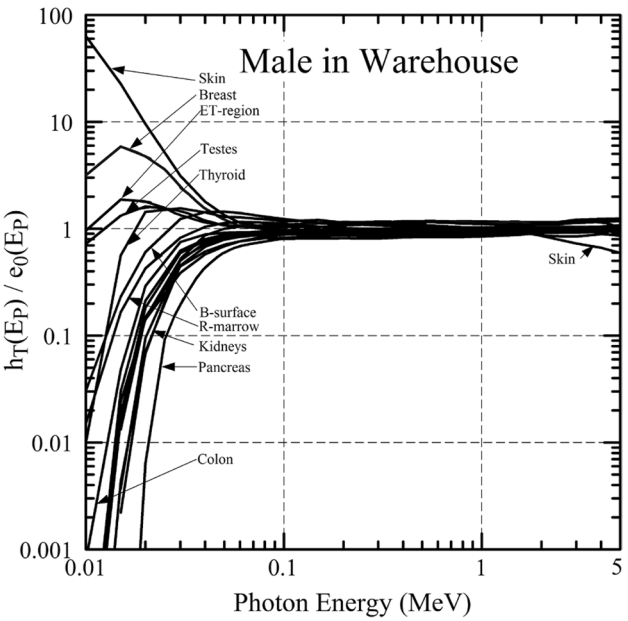

Fig. 7 Ratios of the organs and tissues to the effective dose rate for the male phantom in the warehouse

The organ and tissue dose rate coefficients used to determine the effective dose rate are available on the CRPK website (https://www.ornl.gov/crpk) or by contacting the authors. Figure 6 shows the maximum and minimum dose

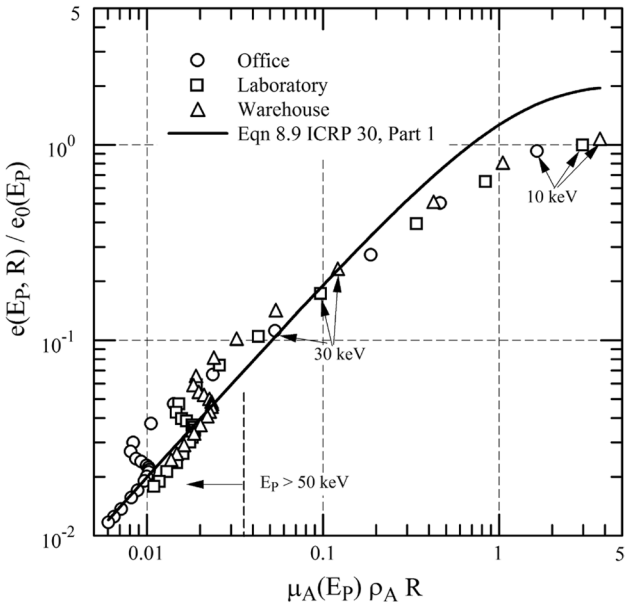

Fig. 8 Effective dose rate coefficient for exposure to airborne photon emitters of energy E_P in a room of effective radius R, to photons of energy E_P as determined by Eq. 8.9 of ICRP Publication 30 (ICRP 1979) compared to the values determined in this work for the office, laboratory, and warehouse

rate coefficients for specific organs and tissues as a function of photon energy for the male phantom in the warehouse. Figure 7 shows the ratios of the various organs and tissues to the effective dose rate for the male phantom in the warehouse.

The ICRP Publication 30 methodology derived dose rates to tissues of the body due to occupational submersion exposure in three rooms by an approximate adjustment of dose rate coefficients for semi-infinite cloud exposures. In today's terminology, Eq. 8.9 of Publication 30 (ICRP 1979) expresses the effective dose rate coefficient, $\dot{e}(E_P, R)$, for exposure to airborne photon emitters of energy E_P in a room of effective radius R as:

$$\dot{e}(E_P, R) = 2\dot{e}_0(E_P)\left[1 - e^{(-\mu_A \rho_A R)}\right], \quad (4)$$

where $\dot{e}_0(E_P)$ is the effective dose rate for a semi-infinite cloud. The factor of 2 was applied as some tissues irradiated in the room are not limited to a 2π geometry, μ_A is the mass energy absorption coefficient in air, ρ_A is the density of air, and R is the effective radius of the room. The effective radius is the radius of a sphere with a volume equal to that of the room. For the rooms considered in the present work, the ratio of the effective dose rate in the room to that for a semi-infinite exposure is compared with predictions of Eq. 4 in Fig. 8. The maximum error in the ICRP 30 approximation occurs at low photon energy; at 10 keV the dose rate is overestimated by about 90%. The approximation underestimates the dose rate for photons of energies between 40 and 1000 keV by about 50%. At about 1000 keV, the error is typically less than 10%.

Conclusion

Dose rate coefficients for three room sizes representing an office, laboratory, and warehouse have been reported. The coefficients for electrons exhibit little dependence on room size for most energies. The photon dose rate coefficients vary based on room size as a result of their longer mean free path and differ from the semi-infinite case reported previously. Differences in noble gas dose rate coefficients between the office and warehouse range from a factor of one for radionuclides such as Ar-42 and Kr-85 to as high as 2.2 for Rn-220 and Kr-76. The approximate formulation for occupational submersion exposure in rooms used in ICRP Publication 30 is found to be inadequate for the rooms considered in this work.

Acknowledgement The authors express their thanks to Nina Petoussi-Henss for providing a table of the mono-energetic photon effective dose rate coefficients reported in Petoussi-Henss et al. (2012).

Compliance with ethical standards

Conflict of interest The authors declare that they have no conflict of interest.

References

Bellamy MB, Veinot KG, Hiller MM, Dewji SA, Eckerman KF, Easterly CE, Hertel NE, Leggett RW (2016) Effective dose rate coefficients for immersions in radioactive air and water. Radiat Prot Dosim 174(2):275–286

ENDF-6 (2005) Formats manual. In: Herman M (ed) ENDF/B-VI Release 8, BNL-NCS-44945-05-Rev., National Nuclear Data Center Brookhaven National Laboratory, Upton, N.Y. 11973-5000

International Commission on Radiological Protection (1977) Recommendations of the ICRP. ICRP Publication 26. Pergamon Press, Oxford

International Commission on Radiological Protection (1979) Limits for intakes of radionuclides by workers. ICRP Publication 30. Pergamon Press Inc., Elmsford

International Commission on Radiological Protection (1991) 1990 Recommendations of the international commission for radiological protection. ICRP Publication 60. Pergamon Press, Oxford

International Commission on Radiological Protection (2002) Basic anatomical and physiological data for use in radiological protection reference values. ICRP Publication 89. Ann ICRP 32(3–4), Pergamon Press

International Commission on Radiological Protection (2007) The 2007 recommendations of the international commission on radiological protection. ICRP publication 103. Ann ICRP 37(2–4), Elsevier

International Commission on Radiological Protection (2008) Nuclear decay data for dosimetric calculations. ICRP Publication 107. Ann ICRP 38(3), Elsevier

International Commission on Radiological Protection (2009) Adult reference computational phantoms. ICRP Publication 110. Ann ICRP 39(2), Elsevier

International Commission on Radiological Protection (2010) Conversion coefficients for radiological protection quantities for external radiation exposures. ICRP Publication 116. Ann ICRP 40(2–5), Elsevier

McConn Jr. RJ, Gesh CJ, Pagh RT, Rucker RA, Williams III RG (2011) Compendium of material composition data for radiation transport modeling PIET-43741-TM-963/PNNL-15870, Rev. 1. Pacific Northwest National Laboratory

MCNP6 (2013) USER'S MANUAL Version 1.0. In: Pelowitz DB (ed) LA-CP-13-00634 Rev. 0, Los Alamos National Laboratory Los Alamos, New Mexico

Petoussi-Henss N, Schlattl H, Zankl M, Endo A, Saito K (2012) Organ doses from environmental exposures calculated using voxel phantoms of adults and children. Phys Med Biol 56:5679–5713

Ryman JC, Faw RE, Shultis K (1981) Air-ground interface effect on gamma-ray submersion dose. Health Phys 41(5):759–768

Veinot KG, Eckerman KF, Bellamy MB, Hiller MM, Dewji SA, Easterly CE, Hertel NE, Manger R (2017) Effective dose rate coefficients for exposure to contaminated soil. Rad Environ Biophys 56(3):255–267